ADVANCED SUSTAINABLE SYSTEMS
www.advsustainsys.com

Bimetallic Intersection in PdFe@FeO_x-C Nanomaterial for Enhanced Water Splitting Electrocatalysis

*Jordan Martinez, Jaime Mazarío, José Luis Olloqui-Sariego, Juan José Calvente, Mohanad D. Darawsheh, Guillermo Mínguez-Espallargas, Marcelo E. Domine, and Pascual Oña-Burgos**

Supported Fe-doped Pd-nanoparticles (NPs) are prepared via soft transformation of a PdFe-metal oraganic framework (MOF). The thus synthesized bimetallic PdFe-NPs are supported on FeO_x@C layers, which are essential for developing well-defined and distributed small NPs, 2.3 nm with 35% metal loading. They are used as bifunctional nanocatalysts for the electrocatalytic water splitting process. They display superior mass activity for the oxygen evolution reaction (OER) and the hydrogen evolution reaction (HER), both in alkaline and acid media, compared with those obtained for benchmarking platinum HER catalyst, and ruthenium, and iridium oxide OER catalysts. PdFe-NPs also exhibit outstanding stability against sintering that can be explained by the protecting role of graphitic carbon layers provided by the organic linker of the MOF. Additionally, the superior electrocatalytic performance of the bimetallic PdFe-NPs compared with those of monometallic Pd/C NPs and FeO_x points to a synergetic effect induced by Fe–Pd interactions that facilitates the water splitting reaction. This is supported by additional characterization of the PdFe-NPs prior and post electrolysis by TEM, XRD, X-ray photoelectron spectroscopy, and Raman revealing that dispersed PdFe NPs on FeO_x@C promote interactions between Pd and Fe, most likely to be Pd–O–Fe active centers.

1. Introduction

Developing new energy sources with renewability, sustainability, and cleanness is mandatory considering the increasing energy consumption and environmental pollution. In that direction, hydrogen has received much attention due to its zero-emission properties and high energy density, and it can be electrochemically generated from water splitting driven by renewable and intermittent power sources.[1–5] In fact, water splitting is one of the most critical processes for many applications associated with carbon-free energy storage and conversion, such as rechargeable metal–air batteries and regenerative fuel cells.[6–9] Up to now, there are two leading water-splitting technologies in industrial applications, one acidic water electrolyzer integrated with a polymer electrolyte membrane and the other alkaline water electrolyzer.[10,11] This process combines two half-cell reactions to produce hydrogen and oxygen gases, namely the Hydrogen Evolution Reaction (HER) at the cathode and the Oxygen Evolution Reaction (OER) at the anode..

Nevertheless, water splitting is a strenuous reaction, with a thermodynamic voltage of 1.23 V,[12,13] which is strongly influenced by the slow kinetics, large overpotential for both reactions, and long-term stability.[14–16] Therefore, the requirement of efficient electrocatalysts for both HER and OER is indispensable to overcome these setbacks in water splitting. The benchmark HER electrocatalysts are platinum (Pt)-based materials, but these are not good for OER, whereas iridium and ruthenium oxides are the state-of-art OER electrocatalysts. Unfortunately, they show insufficient activity toward HER.[17] Additionally,

J. Martinez, J. Mazarío, M. E. Domine, P. Oña-Burgos
Institute of Chemical Technology
Polytechnic University of Valencia-Superior Council of Scientific Investigations (UPV-CSIC)
Avda. de los Naranjos s/n, Valencia 46022, Spain
E-mail: pasoabur@itq.upv.es

The ORCID identification number(s) for the author(s) of this article can be found under https://doi.org/10.1002/adsu.202200096.

DOI: 10.1002/adsu.202200096

J. L. Olloqui-Sariego, J. J. Calvente
Department of Chemistry and Physics
University of Sevilla
Profesor García González 1, Sevilla 41012, Spain

M. D. Darawsheh, G. Mínguez-Espallargas
Molecular Science Institute (ICMol)
University of Valencia
c/Catedrático José Beltrán, 2, Paterna 46980, Spain

P. Oña-Burgos
Department of Chemistry and Physics
University of Almería
Ctra. Sacramento, s/n, Almería E-04120, Spain

the rocketing price and the scarcity of their components are two major obstacles against their practical implementation.[6–8] Besides, combining a first-row transition metal such as Ni or Co with noble metals has been successfully employed to achieve multifunctional catalysts for HER/OER.[18–22] Recently, several works have indicated that heterometallic M–M′O_xH_y {hydr(oxy)oxide}intermediates (FeNi, FeCo, among others)[23–29] improve the OER catalytic activity versus homometallic systems, based on charge delocalization between metal centers.[24] In this direction, balancing Fe dissolution and redeposition rates over a MO_xH_y host establishes dynamically stable Fe active sites.[24] In addition, by varying the Fe content of the electrolyte, it has been proven the key role of the strong interaction of Fe with the MO_xH_y host in the control of the average number of Fe active sites present at the solid/liquid interface.[24] Therefore, the increase in Fe–M interactions will be reflected in an immediate improvement of the electrocatalytic OER activity.

In that context, we have recently shown a soft and tailored transformation of a PdFe-MOF into Fe-doped Pd-NPs supported on nanoclusters of FeO_x@C (PdFe@FeO_x-C), improving the nature of the generated material against other synthetic strategies.[30] Furthermore, the synthesis set-up toward carbon-supported PdFe nanoparticles (NPs) involves improving the tailoring of Chaudret's procedure based on the use of an amine (aniline) in the presence of hydrogen (H_2), in order to reduce metallic species and to lead to NP formation.[31–33] Our modified approach consists of the in situ generation of the amine (i.e., aniline), instead of using it as a solvent, to provide the reaction mixture with a slow supply of amine.[30] It results in a slowly generated heterometallic nanomaterial, thereby providing a well-controlled and reproducible material comprising both metallic NPs and FeO_x-doped graphitic support. In the previous manuscript, the catalytic activity of this material on a nitroarene hydrogenation reaction was tested, noticing an enhancement of activity due to the bimetallic nature of our material, which presents an intimate interaction between its metallic components.[31] As a result of this combination of metallic functionalities, the as-synthesized PdFe@FeO_x-C nanomaterial offers exciting opportunities to conduct the electrocatalytic water splitting process. Indeed, introducing a second metal, especially a non-noble transition metal, would produce a synergetic effect that modifies the surface properties of Pd catalyst, thereby modulating the adsorption energy of hydrogen or oxygen intermediates, increasing the active sites, and ultimately improving the catalyst performance.[34] This soft methodology allows a tailored control of NP size (at least six times smaller with similar metal loading) and stronger bimetallic nature of the material with respect to the most common strategy based on MOFs pyrolysis.[35–37]

Although PdFe electrocatalysts have been widely studied in ORR[38] and HER[39] (both reduction reactions), their application as bifunctional pH-universal electrocatalysts for overall water splitting has not been successfully attempted to the best of our knowledge. In this sense, the herein synthesized ultrasmall PdFe-NP (2.3 nm with 35% of metal loading), having a vast number of Fe–Pd interactions,[30] is a good candidate to be HER active, while nanometric iron oxide is expected to be OER active. Accordingly, we have employed this bimetallic nanomaterial to build electrodes and evaluate its performance for the half-reactions involved in water splitting (HER/OER). The resulting electrodes are contrasted structurally and catalytically with monometallic Pd and Fe NPs. Besides, the electrode stability was assessed by measuring leaching and employing long-term experiments and different characterization techniques of the postcatalysis electrodes to correlate the catalyst structure with catalytic activity and stability. As a result, we demonstrate the superior performance of the PdFe@FeO_x-C nanomaterial as a bifunctional and pH-universal catalyst for electrocatalytic water splitting.

2. Results and Discussion

2.1. Structural Characterization of the PdFe@FeO_x-C@Nafion Composite

The experimental procedure and those physicochemical transformations involved in the synthesis of PdFe-MOF precursor and its subsequent chemical transformation to yield the desired PdFe@FeO_x-C nanomaterial were thoroughly described in our previous work.[31] Nonetheless, specific experimental details used in this work can be found in Section SB, Supporting Information.

To fabricate an electrode for electrocatalytic water splitting, we deposited onto a graphite electrode a nanocomposite prepared by dispersing the palladium-iron nanoparticles (PdFe-NPs) supported on an iron oxide-doped carbon (FeO_x-C) nanomaterial (PdFe@FeO_x-C), with Nafion polymer. Prior to electrochemical interrogation, we compared the nature of each material, bimetallic nanomaterial, and its nanocomposite, and checked the stability of the nanocomposite throughout the incorporation of Nafion during electrode fabrication by microscopy (HR-TEM), X-Ray powder diffraction, and selected area electron diffraction (SAED). **Figure 1** summarizes the structural characterization of each material.

Electron microscopy techniques reveal that the in situ synthesized PdFe@FeO_x-C nanomaterial from PdFe-MOF results in ultrasmall PdFe-NPs with a very narrow distribution and an average size of 2.3 ± 0.5 nm (Figure 1a,b), embedded in a graphitic carbon doped by FeO_x. Notably, upon dispersion of this nanomaterial in Nafion, the nature of the PdFe-NPs in the nanocomposite remains unchanged with an average NP size of 2.7 ± 1.0nm (Figure 1e,f). As previously reported, the small size of the PdFe-NPs is consistent with the heterometallic nature of the NPs.[40] The presence of Fe in nanomaterial and nanocomposite is evidenced by measuring the interplanar distances by TEM (Figure 1c,g). In fact, the interplanar distances of the electron diffraction patterns indicate the absence of undesired homometallic Pd crystalline phases in both nanomaterial and nanocomposite (Figures 1d and 1h, respectively).

Moreover, the formation of bimetallic NPs is further confirmed by their similar XRD patterns (Figure 1i). Both XRD patterns match well with the standard PDF card of the PdFe intermetallic phase (#00-002-1440). Besides, no impurities corresponding to metallic iron or palladium oxide are detected. Likewise, an iron oxide signal (magnetite; Fe_3O_4) is detected in PdFe@FeO_x-C with very low intensity (at 36°), and not observed in the case of PdFe@FeO_x-C/Nafion. Since EDAX mapping of the nanocomposite in Figure S3, Supporting

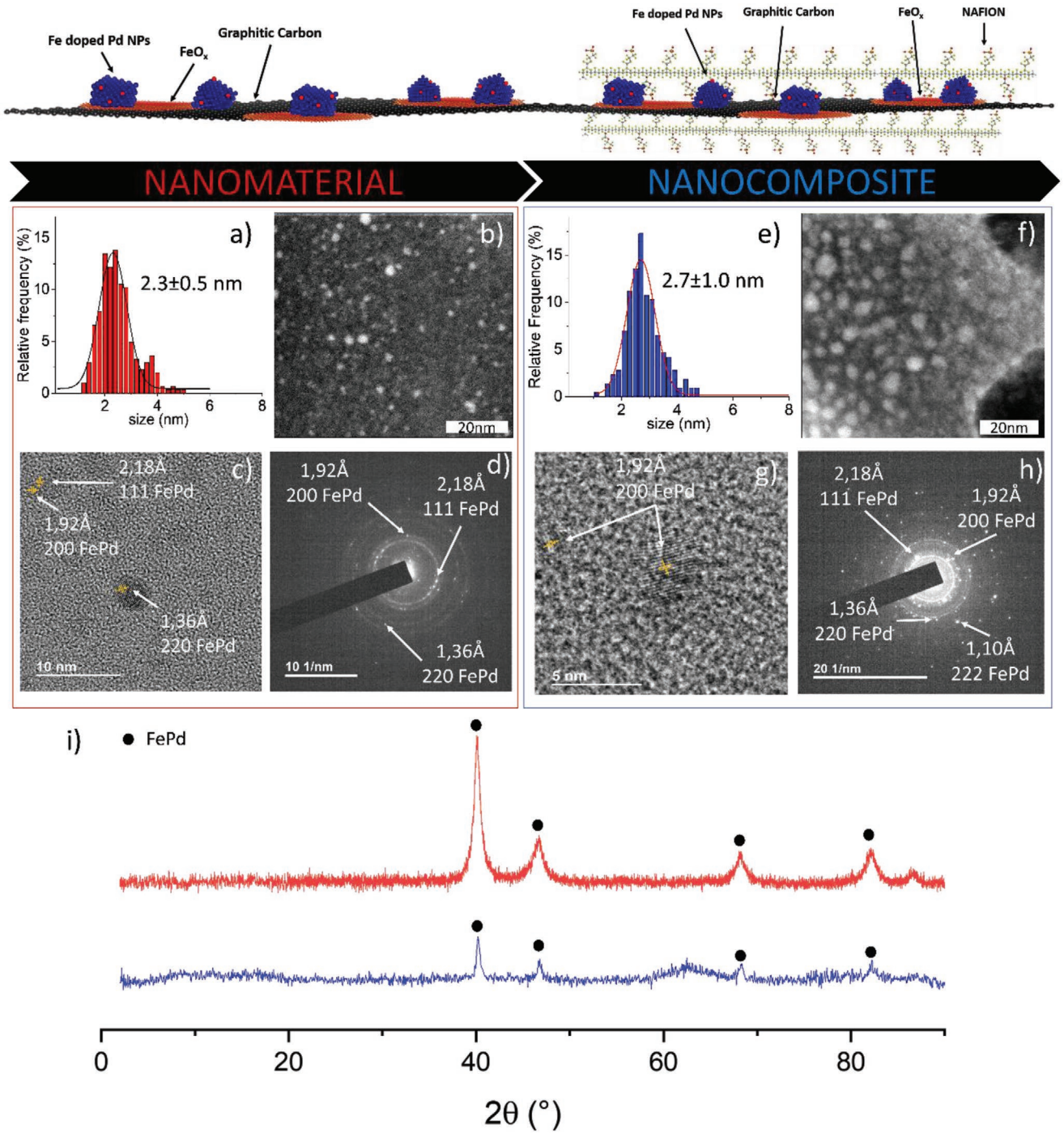

Figure 1. a) Particle size distribution, b) HR-STEM micrograph, c) TEM image with measured interplanar distances, and d) SAED patterns, respectively, of PdFe@FeO_x-C nanomaterial. e) Particle size distribution, f) HR-STEM micrograph, g) TEM image with measured interplanar distances, and h) SAED patterns, respectively, of the corresponding PdFe@FeO_x-C/Nafion nanocomposite. i) XRD patterns of PdFe@FeO_x-C (red), and PdFe@FeO_x-C/Nafion (blue), respectively. For zoom of Figures 1c,d and 1g,h, see Figures S4 and S5, Supporting Information, respectively.

Information, reveals that small iron oxides clusters are present in large amounts in the carbon matrix, this phenomenon is the consequence of some larger iron oxide NPs, which is doping the carbonaceous part of the nanomaterial.

Raman spectroscopy of the PdFe@FeO_x-C/Nafion nanocomposite (Figure S1a, Supporting Information) confirms the presence of iron oxide with a peak around 631 cm^{-1}, ascribed to magnetite.[41] In addition, the presence of a set of characteristic peaks of graphitic carbon (Figure S2, Supporting Information) at 1599 cm^{-1} (G band) and around 1300 cm^{-1} (D band) can be observed. The intensity ratio between the D and the G bands (I_D/I_G) provides the degree of crystallinity and carbon disorder.

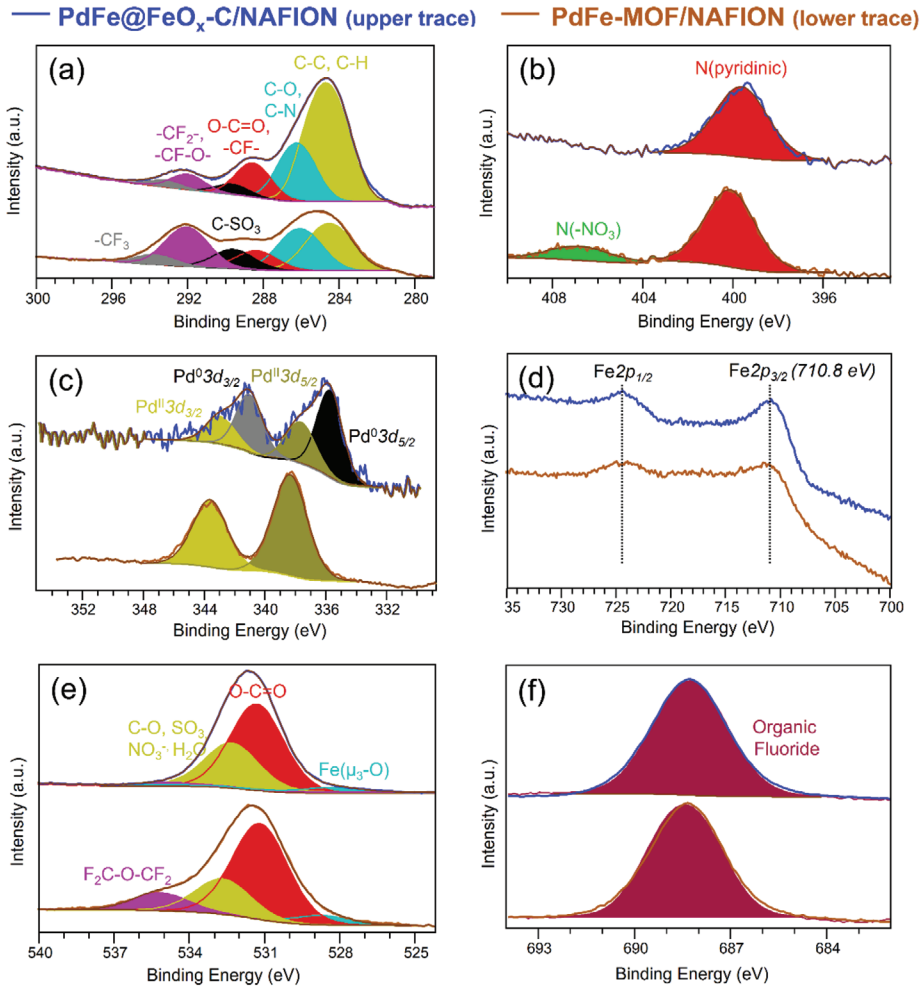

Figure 2. a) C1s, b) N1s, c) Pd3d, d) Fe2p, e) O1s, and f) F1s XPS regions of PdFe-MOF/Nafion and PdFe@FeO_x-C/Nafion.

A value of I_D/I_G = 0.86 was estimated, consistent with a disordered graphitic carbon in the nanocomposite.[42] Finally, the chemical composition of the nanomaterial was determined by using inductively coupled plasma emission spectrometry, establishing a composition of 15.2 wt% of Pd and 20.6 wt% of Fe in the bimetallic PdFe-NP, slightly differing from those of the original MOF precursor (Table S1, Supporting Information).

Furthermore, the electronic structure of the PdFe@FeO_x-C/Nafion nanocomposite was also analyzed by X-ray photoelectron spectroscopy (XPS) and compared with that of a composite containing the precursor PdFe-MOF (**Figure 2**).

Because of immobilization on Nafion, the C1s region (Figure 2a) shows a complex group of signals needing several contributions to fit the spectra. Due to the complex nature of the C1s region, and the likelihood of having contributions from Csp^2 and Csp^3, the charge corrections of the spectra were done against Nafion $-CF_2-$ carbon (C1s, 292.0 eV). Based on that, the C—C, C—H signal (adventitious carbon and carbon skeleton of MOF and nanomaterial) appears at ≈284.6 eV. At around 286 eV, C bonded to N can be found together with the C—O from the adventitious carbon and, at ≈288.5 eV, the signal combines contributions from carboxylates and the Nafion —CF— unit. At higher B.E., signals are to correspond to other Nafion structural units (i.e., $C-SO_3$, $-CF_2-$, —CF—O, and $-CF_3$).[30,43–45]

In the case of N1s (Figure 2b), the signal at 400.1 eV for the MOF should be due to the pyridinic ligand coordinated to Pd, thereby shifted at higher B.E. than expected. This fact has been previously observed for coordinated and/or protonated pyridine derivatives.[46–48] In the PdFe@FeO_x-C nanocomposite, the B.E. decrease of this N (399.7 eV) is explained based on the partial exit of the ligand from the Pd coordination sphere. This pyridinic N would likely be doping the graphitic carbonaceous support, previously detected by Raman. Besides, for PdFe-MOF, a signal at 406.7 eV can be seen, corresponding to N of the nitrate counterion in the MOF.[49]

As shown in Figure 2c, the Pd3d region points out Pd(II) in the MOF with a doublet at 338.2 and 343.5 eV. It should be indicated that the positive shift in Pd(II) position is likely implying coordination to Cl (Figure S7a, Supporting Information, confirms Cl presence).[50] Conversely, the PdFe@FeO_x-C nanocomposite shows two different contributions for $Pd3d_{5/2}$ at 335.8 and 337.7 eV, corresponding to Pd^0 and surface PdO, respectively.[51] Importantly, we previously proved

the $Pd3d_{5/2}$ at the PdFe-NP shifted toward lower binding energies than what is usually observed for Pd^0 due to a charge transfer from either the Fe in the NP or the FeO_x in the support.[31] Nevertheless, the effect of the Nafion-fluorinated chains on Pd is likely to be distorting its electronic environment and upshifting these B.E.,[52,53] thereby counteracting the former effect.

Concerning the Fe2p region (Figure 2d), considering that Fe(III) and Fe(II) are very close to each other and the likely presence of a complex multiplet splitting structure, the result of a peak fitting for laboratory-scale XPS studies might be too adventurous as to be somehow reliable. Nonetheless, it is noteworthy that $Fe2p_{1/2}$ and $Fe2p_{3/2}$ maxima positions are susceptible to the oxidation states of iron. For these samples, the maxima of the Fe2p photoelectron peaks appeared around 710.8 and 724.3 eV, respectively. The separation of the 2p doublet is then 13.5 eV. These aspects suggest Fe(III) associated with oxygen as the predominant species, although a shoulder at lower B.E. might indicate the presence of iron in lower oxidation states.[54–56]

Regarding the O1s region (Figure 2e), different contributions from Nafion and either the MOF or the nanocomposite could be identified. When we described the MOF structure previously, the weak signal at ≈528.5 eV was ascribed to the oxo bridge between three irons, being mostly preserved in the derived nanocomposite.[30,57,58] At ≈531.0–531.5 eV, the signal observed for the PdFe-MOF comes from the carboxylates coordinated to iron.[59,60] The signal between 532 and 533 eV is due to several contributions such as nitrate ions (in the MOF),[61] water molecules,[44] and oxygen from the Nafion sulfonic group.[62] Finally, the higher B.E. signal (534.9–535.1 eV) corresponds to the fluorinated ether group (shifted toward lower B.E. because of a potential contribution from residual water and/or nitrates).[62] F1s XPS signal appears at 688.1–688.4 eV (Figure 2f, organic fluorines).[44] Last, Figure S7b, Supporting Information, confirms the presence of S after Nafion incorporation, with an S2p feature at ≈169.5 eV corresponding to organic sulfate.[63]

2.2. Electrocatalytic Performance of $PdFe@FeO_x$-C Composite for Hydrogen/Oxygen Involving Reactions

2.2.1. Electrocatalytic HER and OER

The electrocatalytic activity of the $PdFe@FeO_x$-C nanomaterial toward overall water splitting was assessed from the HER and OER polarization curves measured in acid and alkaline media by means of rotating disk voltammetry (**Figure 3**). For comparative purposes, we have also measured the polarization curves of the benchmarking HER catalyst platinum (NPs with 5 wt% metal loading), and OER catalysts ruthenium and iridium oxides. First, we estimated the roughness factor of the electrodes prepared with the different nanomaterials by

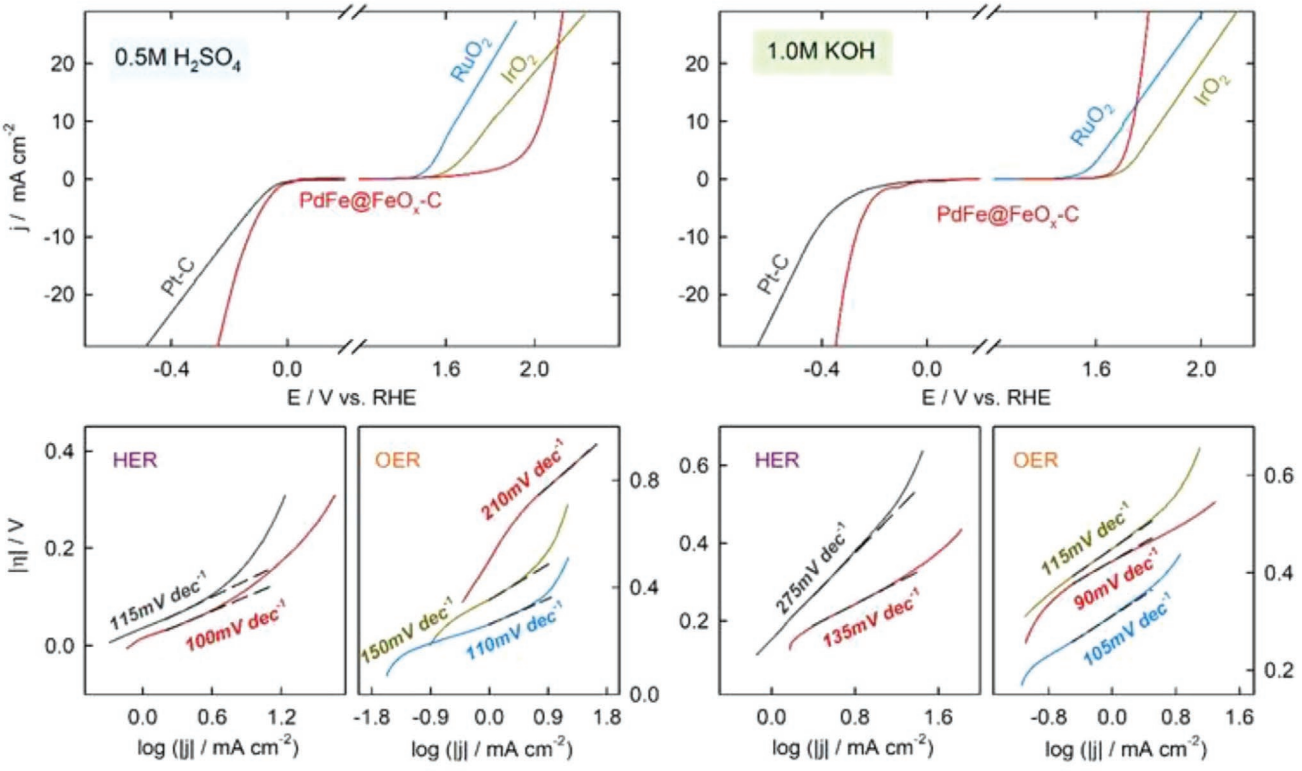

Figure 3. (Top panel) HER and OER polarization curves recorded at 5 mV s^{-1} and 1500 rpm of the indicated nanomaterials, all of them cross-linked with Nafion deposited in a pyrolytic graphite electrode at the indicated electrolytic aqueous solution at 25 °C. (Bottom panel) Their corresponding Tafel plots.

comparing their differential capacity values (C_{dl}), obtained in the non-Faradaic region, with that measured for the electrode coated solely with Nafion (Figure S10, Supporting Information). All electrodes rendered a roughness factor within the range 1.6–3.3.

The kinetic and thermodynamic metrics for the electrocatalysis of HER and OER by the different nanomaterials are summarized in Figure 3. Indeed, the OER and HER kinetics were drawn from the Tafel slopes of the standard overpotential η ($\eta = E - E^{\circ}$) versus log j plots depicted in Figure 3, as a semiquantitative metrics to predict how much faster the reaction occurs in the presence of the electrocatalysts, and to provide a clear view of its dependence on the applied overpotential. Additionally, Tafel slopes were also determined from the steady-state current density data measured with potentiostatic chronoamperometry with potential steps of 0.01 V and 60 s (Figure S11, Supporting Information).

Starting with the HER, it can be seen that for both acid and alkaline media, our PdFe@FeO_x-C nanomaterial displays lower Tafel slopes than the state-of-the-art Pt. Besides, in agreement with previous data, Pt NPs show higher Tafel slope as pH increases which is consistent with the presence of additional intermediate steps involving water dissociation as a proton source in alkaline media.[64] Indeed, the predominant HER mechanism, based on the Tafel slope values of 96 and 110 mV dec^{-1} in the alkaline and acid media, respectively (Figure S11, Supporting Information), is consistent with a Volmer–Heyrovsky pathway, including a primary discharge step followed by an electrochemical desorption step.[65] The difference between the alkaline and acidic mechanism is the nature of the proton source, namely H_2O or H_3O^+, respectively.[66] Notably, the Tafel slope obtained for PdFe@FeO_x-C catalyst at the strongly alkaline medium approaches that of the acid medium and is significantly lower than that obtained for Pt, indicating that PdFe@FeO_x-C exhibits superb HER kinetics at alkaline pH. This can be attributed to the hybrid nature of the catalyst that has an active component for water dissociation (iron oxide), in such a way that its incorporation may increase the HER activity of its counterpart, in our case palladium.[67,68] In addition, the bimetallic nature of the material is expected to promote a synergetic effect, thus facilitating the HER kinetics of PdFe@FeO_x-C electrocatalyst (see below). Moreover, a nitrogen-doped carbon substrate surface originating from the MOF transformation could also bring added benefits by facilitating hydrogen intermediates adsorption/desorption that enhanced the HER activity of the nanomaterial.[69–71]

For the OER, two Tafel slopes are clearly distinguishable at low and high overpotentials, indicating that the individual steps of the electrocatalytic OER mechanism are potential dependent, which are intimately related to the rate-determining step (RDS).[72] In the lower overpotential region, where the potential-determining step is the metal–hydroperoxide intermediate formation,[73] the PdFe@FeO_x-C nanomaterial exhibits a higher Tafel slope than IrO_2 and RuO_2 in the acid medium, whereas it becomes lower at the alkaline solution. In addition, in the higher overpotential region, where the RDS is the hydroxide coordination coupling to the catalyst oxidation, the polarization curves of PdFe@FeO_x-C clearly evidence steeper dependence of the current density with overpotential in all media, which ultimately means lower Tafel slopes than benchmark IrO_2 and RuO_2 OER catalysts. The latter can be attributed to the multimetallic nature of the PdFe@FeO_x-C nanomaterial that might promote Pd–O–Fe active centers[24] with the appropriate metal—oxygen bond strength and better stabilization of the catalytic intermediates.

In addition, electrochemical impedance spectroscopy measurements have been performed with an AC perturbation of 5 mV in the frequency range 0.1 Hz–100 kHz, to complete the characterization of the HER and OER processes. Figure S11, Supporting Information, shows the corresponding Nyquist plots measured at a high overpotential in the HER and OER region for the acid, neutral, and alkaline solutions. They are characterized by a semicircle, whose diameter provides information on the charge transfer rate. The impedance spectra were quantitatively reproduced with the equivalent circuit shown in the insets of Figure S11, Supporting Information, and the fitting parameter values listed in Table S3, Supporting Information. In the equivalent circuit, R_s is the series resistance, which includes the solution and film resistance, R_{ct} is the resistance to charge transfer, and Q_{dl} stands for the double layer capacitance. The smaller diameter of the semicircles (i.e., the lower R_{ct}) obtained in the alkaline solution for both HER and OER reveals the better electrocatalytic performance of the PdFe@FeO_x-C nanomaterial for the water splitting in this medium.

From an operative point of view, it is interesting to evaluate the water splitting cell overpotential required for high production of hydrogen and oxygen (high current density) from the corresponding HER and OER overpotentials ($|\eta_{cel}| = |\eta_{HER} - \eta_{OER}|$). Bar plots in the top panel of **Figure 4** show the values of $|\eta_{HER}|$ and $|\eta_{OER}|$ for the bifunctional PdFe@FeO_x-C nanomaterial and the monofunctional benchmarking electrocatalysts Pt/C (for HER), and IrO_2, RuO_2 (for OER), measured for a current density of 20 mA cm^{-2}.

The HER overpotential of PdFe@FeO_x-C is smaller than that of Pt/C in both alkaline and acid media, and both increase when passing from acid to alkaline conditions. For the OER process, however, there is a different scenario. In acid conditions, the PdFe@FeO_x-C shows greater overpotential than those obtained with IrO_2 and RuO_2; whereas in alkaline solution, its value is smaller than those obtained with IrO_2 and RuO_2. From the individual values of the HER and OER overpotentials, we quantified water splitting overpotentials for conceptual electrochemical cells built by different combinations of PdFe@FeO_x-C, Pt/C, IrO_2, and RuO_2 as anodic and cathodic electrocatalysts (bar plots in the bottom panel of Figure 4). As can be seen, although in acid conditions the cell with solely the bifunctional PdFe@FeO_x-C nanomaterial (PdFe/PdFe) is not as promising as the Pt-C/RuO_2 cell, the best choice is combining a cathode with PdFe@FeO_x-C (for hydrogen evolution half-reaction) and an anode with RuO_2 (for oxygen evolution half-reaction). In alkaline conditions, however, the most competitive electrochemical cell for water splitting contains only our bifunctional PdFe@FeO_x-C electrocatalyst.

For carbon-based metal NPs catalysts, the mass activity (i.e., the current normalized by metal loading) is an appropriate indicator of the electrocatalytic activity of a catalyst. Accordingly, **Figure 5** shows the corresponding geometric and mass activities at high overpotential, bearing in mind that the metal loading of

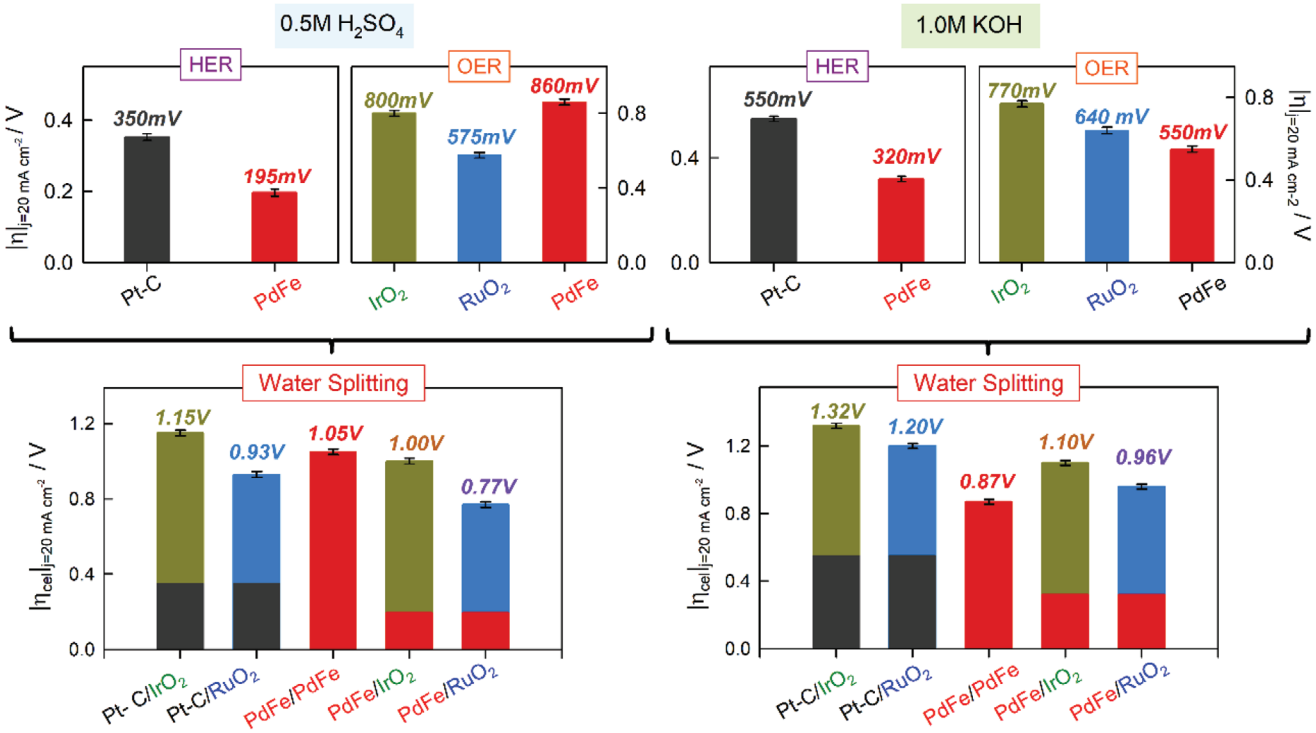

Figure 4. HER and OER (top panel), and water splitting cell (bottom panel) overpotentials at the current density of 20 mA cm^{-2} estimated from their polarization curves recorded at 5 mV s^{-1} and 1500 rpm of the indicated nanomaterials, all of them cross-linked with Nafion deposited in a pyrolytic graphite electrode at the indicated electrolytic aqueous solution at 25 °C.

the PdFe@FeO_x-C, Pt-C, IrO_2, and RuO_2 are 15.2 wt% Pd and 20.6 wt% Fe, 5 wt% Pt, 85.7 wt% Ir, and 75.9 wt% Ru, respectively. Notably, PdFe@FeO_x-C electrocatalyst exhibits substantially higher mass activity for both HER and OER than the commercial benchmarking electrocatalysts. Analogously, the improved intrinsic activity of the active sites in the PdFe@FeO_x-C electrocatalyst

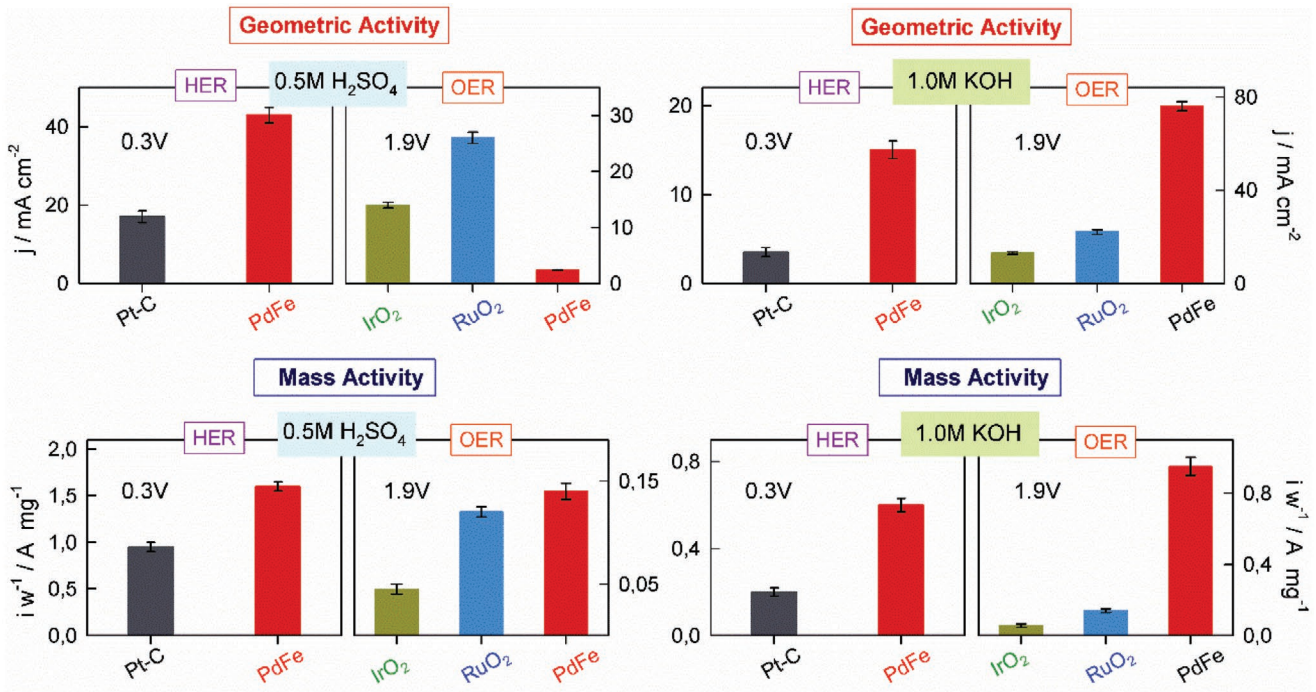

Figure 5. Geometric activity (top panel), and mass activity (bottom panel) for HER and OER at the indicated potential and nanomaterials, all of them cross-linked with Nafion deposited in a pyrolytic graphite electrode at the alkaline and acid electrolytic aqueous solutions at 25 °C.

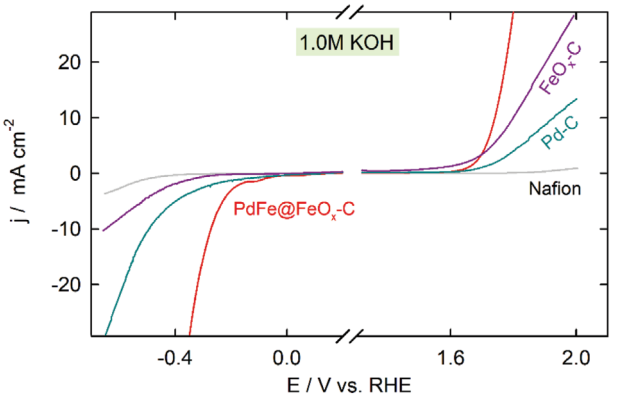

Figure 6. HER and OER polarization curves recorded at 5 mV s^{-1} and 1500 rpm of a pyrolytic graphite electrode modified with the indicated nanomaterial and coated with Nafion in a solution containing 1 M KOH at 25 °C.

can be evidenced from their turnover frequency (TOF) (more details in Supporting Information). Thus, for the HER reduction process, TOF values of 0.90 and 0.35 s^{-1} for PdFe@FeO_x-C and 0.96 and 0.20 s^{-1} for Pt were determined in acid and alkaline conditions, respectively. While, for the OER oxidation process, the PdFe@FeO_x-C electrocatalyst yields TOF values of 0.040 and 0.26 s^{-1} in acid and alkaline conditions, respectively. These values are greater than those obtained for IrO_2 and RuO_2, whose TOF values are 0.022 and 0.031 s^{-1} in the acid medium, and 0.028 and 0.037 s^{-1} in the alkaline medium. Overall, these results reveal the outperformer bifunctional activity of PdFe@FeO_x-C nanomaterial toward electrocatalytic water splitting in terms of favorable overpotential and mass activity at the acid and alkaline media.

2.2.2. Structure–Activity Relationship

To evaluate the role of the multimetallic nature of the PdFe@FeO_x-C nanomaterial on its superb electrocatalytic performance for the overall water splitting, in **Figure 6** we have compared its OER and HER polarization curves at alkaline medium with those of solely Pd NPs (10 wt% metal loading) and FeO_x supported on graphitic carbon (10 wt% metal loading). Notably, PdFe@FeO_x-C clearly exhibits a superior electrocatalytic activity than its single counterparts (Pd-C and FeO_x-C NPs) for both HER and OER, which we speculate may arise from a synergistic electronic interaction between the metallic species of the composite. Indeed, it is well recognized that alloys consisting of a noble metal (–d-electron number greater than –d-orbital number) and a non-noble transition metal (with unpaired d-electrons and unfilled d-orbital) improve the catalytic activity of the precious metal by changing charge distribution.[34] Accordingly, we already proved that Fe-doped Pd NPs have a different charge distribution than pure Pd@C NPs, thus indicating an iron-induced partial charge transfer process.[30] This phenomenon provided increased charge and a better metallic dispersion improving atomic economy. This evidences a change of the average energy of the surface d-band that can modulate the adsorption energy of the catalytic species (hydrogen or oxygen intermediates), which ultimately improves the catalyst performance for water oxidation and reduction.

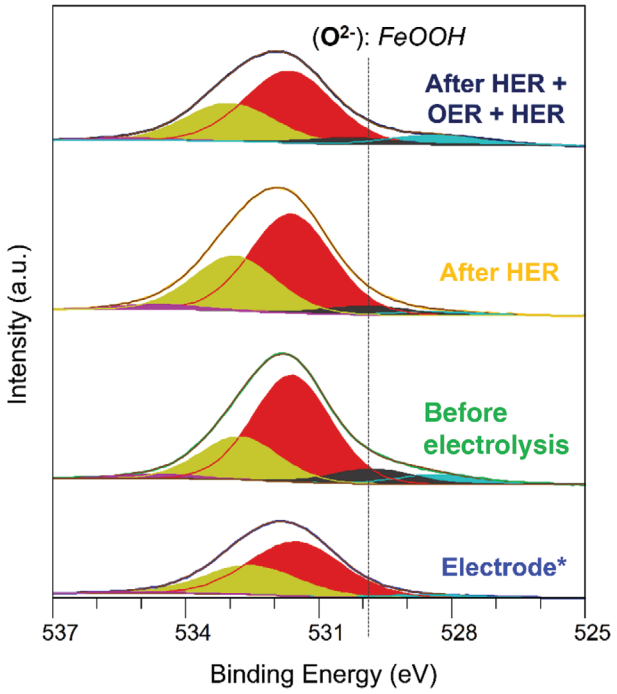

Figure 7. O1s XPS region of the PdFe@FeO_x-C/Nafion composite after the indicated postelectrolysis experiments at a solution containing 1 M KOH. PdFe@FeO_x-C/Nafion composite. Bottom spectra correspond to the composite before use.

In addition, the superior electrocatalytic OER activity of the PdFe@FeO_x-C nanocomposite compared to solely Pd-C and FeO_x-C can be ascribed to a higher number of Fe–Pd interactions, most likely to be Pd–O–Fe. Indeed, it has been recently reported that promoting Fe–metal interactions in Fe–$M^1O_xH_y$ and Fe–$M^1M^2O_xH_y$ hydr(oxy)oxide clusters[23–26] improves the OER catalytic activity versus equivalent homometallic

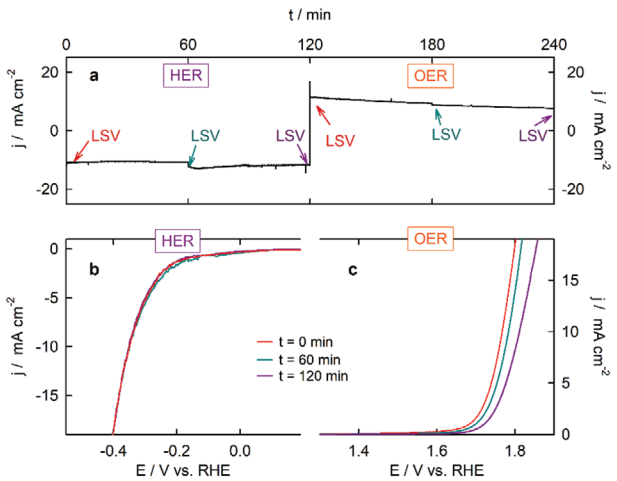

Figure 8. a) Consecutive chronoamperograms at a potential of –0.3 and 1.7 V (vs RHE) for HER and OER processes, respectively, of a pyrolytic graphite electrode modified with PdFe@FeO_x-C nanomaterial in a solution containing 1 M KOH at 25 °C. b,c) Their corresponding rotating disk voltammograms measured at 5 mV s^{-1} and 1500 rpm.

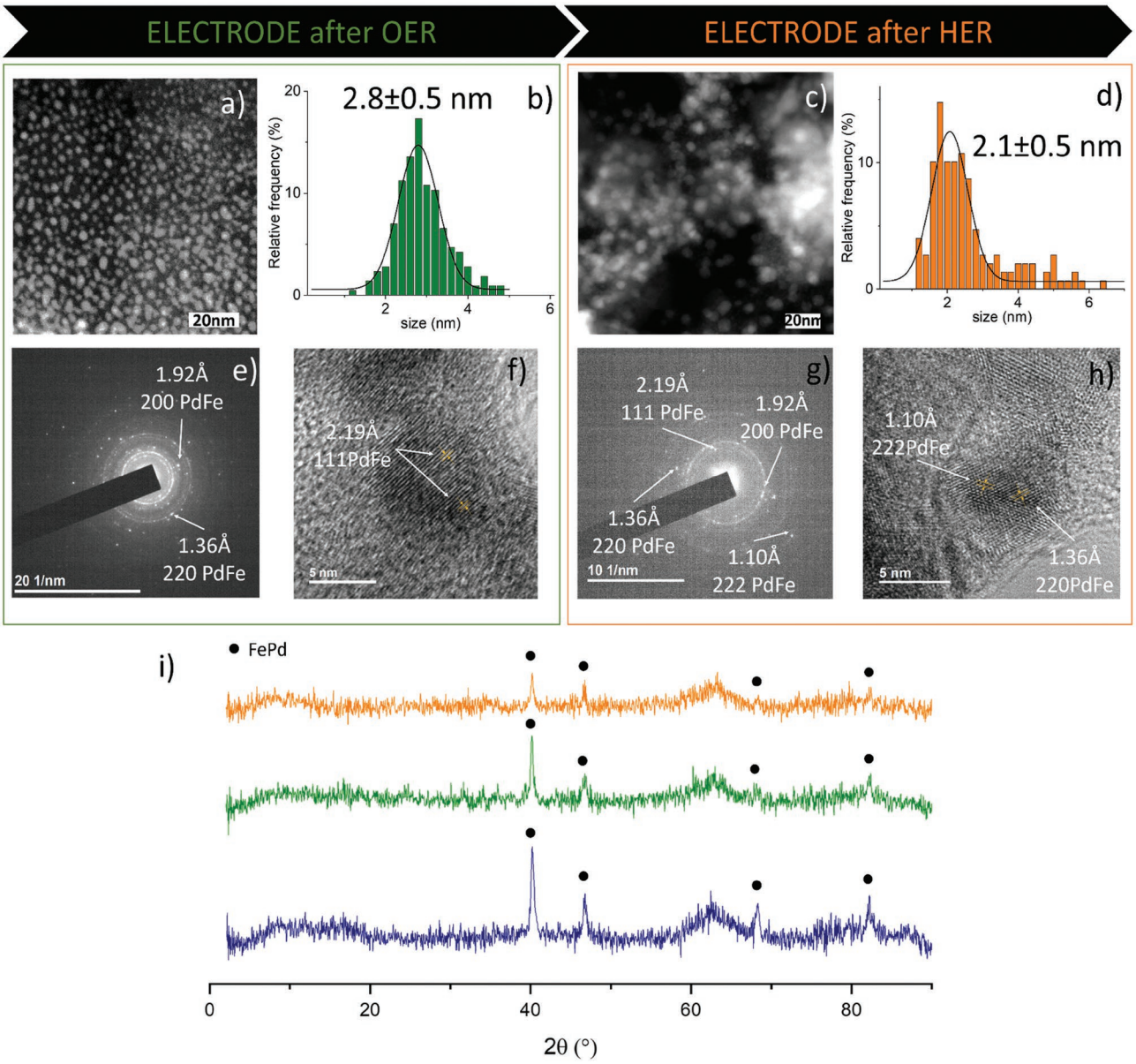

Figure 9. Structural characterization of PdFe@FeO_x-C/Nafion after OER or HER long term electrolysis at a potential of –0.3 and 1.7 V versus RHE, respectively, in a solution containing 1 M KOH at 25 °C; a,c) HR-STEM micrograph image; b,d) Particle size distribution; e,g) SAED patterns; f,h) TEM images; i) XRD patterns (The blue spectra correspond with the XRD pattern of PdFe@FeO_x-C/Nafion before electrolysis).

systems, based on charge delocalization between metal centers.[24] In this line, it has been proposed that a strong interaction of Fe with the MO_xH_y host leads to a higher number of active sites, but also stabilizes these active sites, revealing the crucial role of the Fe–M adsorption energy in the improvement of the OER activity of these materials in alkaline media.

Aiming at further confirming the aforementioned hypothesis about the formation of M_1–O(OH)–M_2 bimetallic intersections in our system, postcatalysis XPS analysis is envisaged as a good tool to examine the effect of the process on the chemical and electronic structure of the PdFe@FeO_x-C nanocomposite (**Figure 7** and Figures S8 and S9, Supporting Information). Interestingly, after being subjected to the OER electrolysis, the nanocomposite presents a significant shift toward lower BE in the $Pd3d_{5/2}$ signal (≈0.5 eV, Figure S9c, Supporting Information), with reference to the original PdFe@FeO_x-C. This kind of displacement suggests electronic changes at the metal components of the nanocomposite during electrode operation.[74,75] This observation might also hint at the idea of the formation of intermetallic species, enhancing OER activity.[23–26] With respect to that possibility, the high BE observed for $Pd3d_{5/2}$ in these materials (≈336.0, and ≈338.0 eV) has been previously associated with Pd–O–Fe bonds.[76] However, these high BEs are also observed before reaction and, as previously stated, they can also be caused by the distortion exerted by the fluorinated

chains of Nafion on Pd and PdO_x electronic structure.[52,53] On another side, if looking at the O1s region more carefully, a new contribution can be seen in the used materials (529.8–530.3 eV, Figure 7), undetected in the fresh catalyst. Since the Fe2p region after reaction (see Figure S9d, Supporting Information) might be attributed to all these potential species, Fe_2O_3, Fe_3O_4, and FeOOH,[55] apart from the remanent Fe(μ_3-O) moieties, this new O1s component is difficult to assign. Nonetheless, the weakening of the broad bands characteristic of FeO_x, and even their disappearance after HER, in the Raman region between 100 and 1000 cm^{-1} (see Figures S1e and S7d, Supporting Information), points at the formation of FeOOH species, with O1s bands at ≈530 eV (O^{2-}, the new band observed) and ≈531.5 eV (OH^-, overlapping with O—C=O).[77,78] Interestingly, this hydroxylated layer on the iron oxides has been described to act as the intermediate in the formation of the Pd—O—Fe bonds.[76]

Therefore, based on the previous experimental data together with reported mechanisms for OER electrocatalysis, we propose that the most active phase of the PdFe@FeO_x-C/Nafion electrodes should be the intermetallic areas between Pd and Fe. In addition, this could also indicate that oxygen—oxygen bond formation takes place preferably through bimetallic rather than monometallic centers.[23–26,79,80] Therefore, the presence of a bimetallic intersection should improve reductive hydrogen adsorption of water, that occurs more efficiently than on other monometallic electrodes already reported.[67,81,82]

2.2.3. Operational Stability

The operational stability and reversibility of the PdFe@FeO_x-C nanostructure during the electrocatalytic OER and HER processes in the alkaline medium have also been assessed by comparing their polarization curves during different times of water electrolysis. In particular, we registered the current intensity in chronoamperometric experiments involving the HER–OER electrolysis cycle that lasted 4 h, with vigorous stirring at 1500 rpm and a fixed potential of –0.3 and 1.7 V versus RHE for water reduction and water oxidation processes, respectively (**Figure 8**a). During HER electrolysis, the current density remains unchanged, closely matching the invariance of their HER polarization curve (Figure 8b). Turning to the electrocatalytic water oxidation reaction, the oxidation current density remains relatively stabilized, with a slight current diminution, which can be attributed to a subtle decrease of the OER electrocatalytic activity as evidenced by their corresponding polarization curves registered during electrolysis (Figure 8c). However, the continuous decrease in the roughness factor of the electrode surface during electrolysis reveals that the decrease in the electrocatalytic OER performance is associated with a loss of the active surface rather than a decrease in the catalyst activity (Figure S12, Supporting Information). These results reveal outstanding operational stability of the PdFe@FeO_x-C nanomaterial.

Further structural characterization by XRD, Raman, and electron microscopy of the electrodes after electrocatalytic reactions were carried out (**Figure 9**). HR-STEM micrograph images of the nanomaterial after OER and HER electrolysis reveal that their size barely changes with an average particle size of

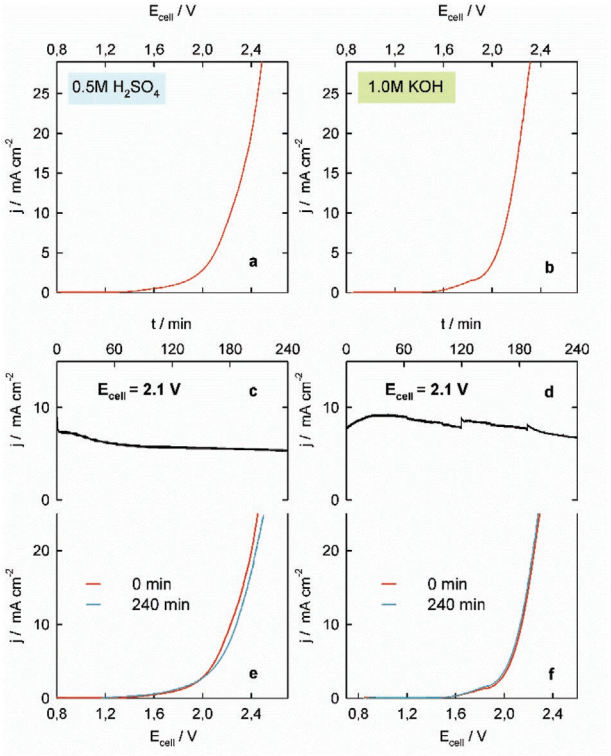

Figure 10. a,b) Polarization curves recorded at 5 mV s^{-1} for the overall water splitting reaction at the indicated aqueous electrolyte solutions and 25 °C in a two-electrode cell containing two pyrolytic graphite electrodes modified with the PdFe@FeO_x-C nanomaterial. c,d) Long-term chronoamperograms measured at 2.1 V, and e,f) their corresponding rotating disk voltammograms measured before (red line) and after (blue line) electrolysis.

2.8 ± 0.5 and 2.1 ± 0.5 nm after OER and HER, respectively. Moreover, SAED patterns and TEM images of the PdFe@FeO_x-C composite after electrolysis experiments, show that the nanomaterial retains their morphology and interplanar distances after electrolysis, as well as their heterometallic character. These results are also supported by XRD, where PdFe@FeO_x-C/Nafion exhibits the same diffraction pattern before and after OER or HER electrolysis.

On the other hand, Raman spectrum after HER is characterized by the disappearance of FeO_x band around 631 cm^{-1} (Figure S6, Supporting Information). Besides, Raman spectrum after OER electrocatalysis indicate that a new oxide band is detected, that can be attributed to the formation of hydr(oxy) oxide species between Pd and Fe, which could be the active OER centers during impressive electrocatalytic water oxidation.[23–26] Furthermore, the reversibility of the PdFe@FeO_x-C/Nafion has also been examined. The structural characterization of the nanocomposite after consecutive HER–OER–HER electrolysis reveals that the electrode has not suffered from any significant change during reactions (Figure S6, Supporting Information). Altogether, these results demonstrate the superb operational stability of the herein produced PdFe@FeO_x-C. In this respect, the N-doped graphitic carbon provided by the organic linker of the MOFs could play a crucial role in the NPs stability against NP sintering.[83–86]

2.3. Electrocatalytic Performance of the PdFe@FeO_x-C Composite for the Water Splitting Reaction

Encouraged by the excellent OER and HER performance of the bifunctional PdFe@FeO_x-C electrocatalyst, we further evaluated its practical application as an anode and cathode for the overall water-splitting reaction in a two-electrode configuration. The polarization curves obtained for the so-assembled electrolytic cell in both 0.5 M H_2SO_4 and 1 M KOH are depicted in **Figures 10**a and 10b, respectively. It turns out that the water splitting starts at the cell voltage of 1.90 and 1.95 V in the acid and alkaline medium, respectively. Furthermore, the PdFe@FeO_x-C-based electrolyzer needs a cell potential of 2.21 V to produce a current density of 20 mA cm^{-2} in 1.0 M KOH, which is less than the voltage required in 0.5 M H_2SO_4 (2.40 V), thus revealing an improvement in the kinetics of water splitting in the alkaline medium.

A long-term chronoamperometric test at 2.1 V for 4 h revealed a negligible decrease of the current density in both media (Figure 10c,d), indicating the excellent stability of the catalyst. Additionally, the invariance of their corresponding polarization curves before and after the electrolysis experiment points to a promising highly active and stable electrocatalyst for the practical overall water splitting (Figure 10e,f).

3. Conclusions

The soft transformation of PdFe-MOF leads to the formation of Fe-doped Pd-NPs supported on FeO_x@C, thus developing a material with well-defined and distributed small particles, which in turn are supported on graphitic carbon layers. Remarkably, this material has been used to build electrodes for HER and OER with substantial higher electrocatalytic performance at wide pH window, in terms of favorable overpotential at high current density, high mass activity, and high stability. The superior performance to solely Pd/C, FeO_x and benchmarking catalytic materials for these reactions clearly points out a positive synergetic effect originated by the multifunctional nature of this catalytic material, that has been proved to rise from the large number of strong interactions between Pd and Fe, most likely to be Pd–O–Fe active centers. Besides, the obtained good electrocatalytic performance of an electrolytic cell based on two electrodes containing the bimetallic Fe-doped Pd-NP indicates that it could be used for practical application in water splitting. This work may provide insights for designing non-noble/noble metal-based alloys as (electro)chemical interfaces that are simultaneously highly active and highly stable.

Supporting Information

Supporting Information is available from the Wiley Online Library or from the author.

Acknowledgements

The authors thank the financial support by the Spanish Government (RTI2018-096399-A-I00). This work has been supported by grants PID2020-117177GB-I00 and CEX2019-000919-M, funded by MCIN/AEI/10.13039/501100011033, Junta de Andalucía (P20_01027 and PYC 20 RE 060 UAL), and the Generalitat Valenciana (PROMETEU2019/066). J. Mazarío thanks the MICINN (CTQ2015-67592) for his Ph.D. scholarship. The authors thank CITIUS-Universidad de Sevilla for providing XPS measurements.

Conflict of Interest

The authors declare no conflict of interest.

Data Availability Statement

The data that support the findings of this study are available from the corresponding author upon reasonable request.

Keywords

electrocatalysis, hydrogen evolution reaction, nanocomposites, oxygen evolution reaction

Received: March 1, 2022
Revised: April 21, 2022
Published online: May 19, 2022

[1] H. Zhang, W. Zhou, J. Dong, X. F. Lu, X. W. (David) Lou, *Energy Environ. Sci.* **2019**, *12*, 3348.
[2] R. Sathre, J. B. Greenblatt, K. Walczak, I. D. Sharp, J. C. Stevens, J. W. Ager, F. A. Houle, *Energy Environ. Sci.* **2016**, *9*, 803.
[3] S. Y. Tee, K. Y. Win, W. S. Teo, L.-D. Koh, S. Liu, C. P. Teng, M.-Y. Han, *Adv. Sci.* **2017**, *4*, 1600337.
[4] C. Xiang, K. M. Papadantonakis, N. S. Lewis, *Mater. Horiz.* **2016**, *3*, 169.
[5] Y. Xu, B. Zhang, *ChemElectroChem* **2019**, *6*, 3214.
[6] J. Zhang, Z. Zhao, Z. Xia, L. Dai, *Nat. Nanotechnol.* **2015**, *10*, 444.
[7] Z. W. Seh, J. Kibsgaard, C. F. Dickens, I. Chorkendorff, J. K. Nørskov, T. F. Jaramillo, *Science* **2017**, *355*.
[8] J. N. Tiwari, K. Nath, S. Kumar, R. N. Tiwari, K. C. Kemp, N. H. Le, D. H. Youn, J. S. Lee, K. S. Kim, *Nat. Commun.* **2013**, *4*, 2221.
[9] L. Li, Z.-w. Chang, X.-B. Zhang, *Adv. Sustainable Syst.* **2017**, *1*, 1700036.
[10] B. Y. Xia, Y. Yan, N. Li, H. B. Wu, X. W. D. Lou, X. Wang, *Nat. Energy* **2016**, *1*, 1.
[11] T. Y. Ma, S. Dai, M. Jaroniec, S. Z. Qiao, *J. Am. Chem. Soc.* **2014**, *136*, 13925.
[12] S. Piccinin, A. Sartorel, G. Aquilanti, A. Goldoni, M. Bonchio, S. Fabris, *Proc. Natl. Acad. Sci. USA* **2013**, *110*, 4917.
[13] Q. Yin, J. M. Tan, C. Besson, Y. V. Geletii, D. G. Musaev, A. E. Kuznetsov, Z. Luo, K. I. Hardcastle, C. L. Hill, *Science* **2010**, *328*, 342.
[14] C. G. Morales-Guio, L.-A. Stern, X. Hu, *Chem. Soc. Rev.* **2014**, *43*, 6555.
[15] S. Bai, C. Wang, M. Deng, M. Gong, Y. Bai, J. Jiang, Y. Xiong, *Angew. Chem.* **2014**, *126*, 12316.
[16] C. Su, T. Yang, W. Zhou, W. Wang, X. Xu, Z. Shao, *J. Mater. Chem. A* **2016**, *4*, 4516.
[17] J. Tian, Q. Liu, A. M. Asiri, X. Sun, *J. Am. Chem. Soc.* **2014**, *136*, 7587.
[18] L. S. Bezerra, G. Maia, *J. Mater. Chem. A* **2020**, *8*, 17691.
[19] X. Wu, C. Tang, Y. Cheng, X. Min, S. P. Jiang, S. Wang, *Chem. - Eur. J.* **2020**, *26*, 3906.

[20] X. Du, Y. Ding, X. Zhang, *Appl. Surf. Sci.* **2021**, *562*, 150227.
[21] X. Du, C. Zhang, H. Wang, Y. Wang, X. Zhang, *J. Alloys Compd.* **2021**, *885*, 160972.
[22] Z. Dai, X. Du, Y. Wang, X. Han, X. Zhang, *Dalton Trans.* **2021**, *50*, 12301.
[23] N. Akbari, I. Kondov, M. Vandichel, P. Aleshkevych, M. M. Najafpour, *Inorg. Chem.* **2021**, *60*, 5682.
[24] D. Y. Chung, P. P. Lopes, P. F. B. D. Martins, H. He, T. Kawaguchi, P. Zapol, H. You, D. Tripkovic, D. Strmcnik, Y. Zhu, S. Seifert, S. Lee, V. R. Stamenkovic, N. M. Markovic, *Nat. Energy* **2020**, *5*, 222.
[25] A. C. Garcia, T. Touzalin, C. Nieuwland, N. Perini, M. T. M. Koper, *Angew. Chem., Int. Ed.* **2019**, *58*, 12999.
[26] P. Chaturvedi, S. Sarker, X. Chen, S. Das, H. Luo, S. N. Smirnov, *ACS Sustainable Chem. Eng.* **2019**, *7*, 11303.
[27] L. Gong, H. Yang, A. I. Douka, Y. Yan, B. Y. Xia, *Adv. Sustainable Syst.* **2021**, *5*, 2000136.
[28] S. Liu, T. Chen, H. Ying, Z. Li, J. Hao, *Adv. Sustainable Syst.* **2020**, *4*, 2000038.
[29] K. Maiti, J. Balamurugan, S. G. Peera, N. H. Kim, J. H. Lee, *ACS Appl. Mater. Interfaces* **2018**, *10*, 18734.
[30] M. D. Darawsheh, J. Mazarío, C. W. Lopes, M. Giménez-Marqués, M. E. Domine, D. M. Meira, J. Martínez, G. M. Espallargas, P. Oña-Burgos, *Chem. - Eur. J.* **2020**, *26*, 13659.
[31] F. Dumestre, B. Chaudret, C. Amiens, P. Renaud, P. Fejes, *Science* **2004**, *303*, 821.
[32] F. Dumestre, B. Chaudret, C. Amiens, M.-C. Fromen, M.-J. Casanove, P. Renaud, P. Zurcher, *Angew. Chem., Int. Ed.* **2002**, *41*, 4286.
[33] C. Pan, K. Pelzer, K. Philippot, B. Chaudret, F. Dassenoy, P. Lecante, M.-J. Casanove, *J. Am. Chem. Soc.* **2001**, *123*, 7584.
[34] F. Shen, Y. Wang, G. Qian, W. Chen, W. Jiang, L. Luo, S. Yin, *Appl. Catal., B* **2020**, *278*, 119327.
[35] R. Wang, X. Sun, S. Ould-Chikh, D. Osadchii, F. Bai, F. Kapteijn, J. Gascon, *ACS Appl. Mater. Interfaces* **2018**, *10*, 14751.
[36] L. Oar-Arteta, M. J. Valero-Romero, T. Wezendonk, F. Kapteijn, J. Gascon, *Catal. Sci. Technol.* **2018**, *8*, 210.
[37] A. Bavykina, N. Kolobov, I. S. Khan, J. A. Bau, A. Ramirez, J. Gascon, *Chem. Rev.* **2020**, *120*, 8468.
[38] X. Tian, X. F. Lu, B. Y. Xia, X. W. (David) Lou, *Joule* **2020**, *4*, 45.
[39] A. Eftekhari, *Int. J. Hydrogen Energy* **2017**, *42*, 11053.
[40] R. Wang, S. Liao, Z. Fu, S. Ji, *Electrochem. Commun.* **2008**, *10*, 523.
[41] D. Bersani, P. P. Lottici, A. Montenero, *J. Mater. Sci.* **2000**, *35*, 4301.
[42] A. C. Ferrari, J. Robertson, *Phys. Rev. B* **2000**, *61*, 14095.
[43] M. V. M. de Yuso, L. A. Neves, I. M. Coelhoso, J. G. Crespo, J. Benavente, E. Rodríguez-Castellón, *Fuel Cells* **2012**, *12*, 606.
[44] NIST X-ray Photoelectron Spectroscopy (XPS) Database, Version 3.5.
[45] J. H. Park, C. H. Lee, J.-M. Ju, J.-H. Lee, J. Seol, S. U. Lee, J.-H. Kim, J. H. Park, J. Ju, J. Lee, J. Kim, C. H. Lee, S. U. Lee, J. Seol, *Adv. Funct. Mater.* **2021**, *31*, 2101727.
[46] H. Li, X. Tan, J. Zhang, *Chin. J. Chem.* **2015**, *33*, 141.
[47] T. Heinrich, E. Darlatt, A. Lippitz, S. Müller, C. A. Schalley, W. E. S. Unger, *J. Electron Spectrosc. Relat. Phenom.* **2019**, *233*, 28.
[48] C. Zhang, J. Li, F. Cheng, *J. Cleaner Prod.* **2020**, *261*, 121114.
[49] J. Seo, A. C. Cabelof, C.-H. Chen, K. G. Caulton, *Chem. Sci.* **2019**, *10*, 475.
[50] M. C. Militello, S. J. Simko, *Surf. Sci. Spectra* **1998**, *3*, 402.
[51] S. Hermans, M. Wenkin, M. Devillers, *J. Mol. Catal. A: Chem.* **1998**, *136*, 59.
[52] A. Gharachorlou, M. D. Detwiler, A. V. Nartova, Y. Lei, J. Lu, J. W. Elam, W. N. Delgass, F. H. Ribeiro, D. Y. Zemlyanov, *ACS Appl. Mater. Interfaces* **2014**, *6*, 14702.
[53] T. Gong, Y. Huang, L. Qin, W. Zhang, J. Li, L. Hui, H. Feng, *Appl. Surf. Sci.* **2019**, *495*, 143495.
[54] T. C. Lin, G. Seshadri, J. A. Kelber, *Appl. Surf. Sci.* **1997**, *119*, 83.
[55] A. P. Grosvenor, B. A. Kobe, M. C. Biesinger, N. S. McIntyre, *Surf. Interface Anal.* **2004**, *36*, 1564.
[56] B. Solsona, T. García, R. Sanchis, M. D. Soriano, M. Moreno, E. Rodríguez-Castellón, S. Agouram, A. Dejoz, J. M. L. Nieto, *Chem. Eng. J.* **2016**, *290*, 273.
[57] T. M. Ivanova, A. V. Shchukarev, R. V. Linko, M. A. Kiskin, A. A. Sidorov, V. M. Novotortsev, I. L. Eremenko, *Russ. J. Inorg. Chem.* **2011**, *56*, 104.
[58] T. M. Ivanova, A. G. Kochur, K. I. Maslakov, M. A. Kiskin, S. V. Savilov, V. V. Lunin, V. M. Novotortsev, I. L. Eremenko, *J. Electron Spectrosc. Relat. Phenom.* **2015**, *205*, 1.
[59] R. Liang, F. Jing, L. Shen, N. Qin, L. Wu, *J. Hazard. Mater.* **2015**, *287*, 364.
[60] M. Zhao, K. Yuan, Y. Wang, G. Li, J. Guo, L. Gu, W. Hu, H. Zhao, Z. Tang, *Nature* **2016**, *539*, 76.
[61] M. Y. Smirnov, A. V. Kalinkin, V. I. Bukhtiyarov, *J. Struct. Chem.* **2007**, *48*, 1053.
[62] M. D. V. M. De Yuso, M. T. Cuberes, V. Romero, L. Neves, I. Coelhoso, J. G. Crespo, E. Rodríguez-Castellón, J. Benavente, *Int. J. Hydrogen Energy* **2014**, *39*, 4023.
[63] A. K. Friedman, W. Shi, Y. Losovyj, A. R. Siedle, L. A. Baker, *J. Electrochem. Soc.* **2018**, *165*, H733.
[64] S. Anantharaj, S. R. Ede, K. Karthick, S. S. Sankar, K. Sangeetha, P. E. Karthik, S. Kundu, *Energy Environ. Sci.* **2018**, *11*, 744.
[65] J. G. N. Thomas, *Trans. Faraday Soc.* **1961**, *57*, 1603.
[66] B. E. Conway, B. V. Tilak, *Electrochim. Acta* **2002**, *47*, 3571.
[67] N. Danilovic, R. Subbaraman, D. Strmcnik, K.-C. Chang, A. P. Paulikas, V. R. Stamenkovic, N. M. Markovic, *Angew. Chem.* **2012**, *124*, 12663.
[68] N. Mahmood, Y. Yao, J. W. Zhang, L. Pan, X. Zhang, J. J. Zou, *Adv. Sci.* **2018**, *5*, 1700464.
[69] Y.-L. Wu, X. Li, Y.-S. Wei, Z. Fu, W. Wei, X.-T. Wu, Q.-L. Zhu, Q. Xu, Y. Wu, X. Li, W. Wei, X. Wu, Q. Zhu, Y. Wei, Q. Xu, Z. Fu, *Adv. Mater.* **2021**, *33*, 2006965.
[70] G. Gao, H. Yu, X. L. Wang, Y. F. Yao, *Mol. Catal.* **2021**, *514*, 111830.
[71] Y. Jiao, Y. Zheng, K. Davey, S. Z. Qiao, *Nat. Energy* **2016**, *1*, 16130.
[72] E. Fabbri, A. Habereder, K. Waltar, R. Kötz, T. J. Schmidt, *Catal. Sci. Technol.* **2014**, *4*, 3800.
[73] S. Anantharaj, S. Noda, M. Driess, P. W. Menezes, *ACS Energy Lett.* **2021**, *6*, 1607.
[74] L. M. R. Gavidia, G. García, D. Anaya, A. Querejeta, F. Alcaide, E. Pastor, *Appl. Catal., B* **2016**, *184*, 12.
[75] H. A. Elazab, S. Moussa, A. R. Siamaki, B. F. Gupton, M. S. El-Shall, *Catal. Lett.* **2017**, *147*, 1510.
[76] R. Muftikian, K. Nebesny, Q. Fernando, N. Korte, *Environ. Sci. Technol.* **1996**, *30*, 3593.
[77] C. R. Brundle, T. J. Chuang, K. Wandelt, *Surf. Sci.* **1977**, *68*, 459.
[78] G. C. Allen, M. T. Curtis, A. J. Hooper, P. M. Tucker, *J. Chem. Soc., Dalton Trans.* **1974**, 1525.
[79] M. S. Burke, L. J. Enman, A. S. Batchellor, S. Zou, S. W. Boettcher, *Chem. Mater.* **2015**, *27*, 7549.
[80] R. L. Doyle, I. J. Godwin, M. P. Brandon, M. E. G. Lyons, *Phys. Chem. Chem. Phys.* **2013**, *15*, 13737.
[81] M. Gong, W. Zhou, M.-C. Tsai, J. Zhou, M. Guan, M.-C. Lin, B. Zhang, Y. Hu, D.-Y. Wang, J. Yang, S. J. Pennycook, B.-J. Hwang, H. Dai, *Nat. Commun.* **2014**, *5*, 1.
[82] M. Gong, D.-Y. Wang, C.-C. Chen, B.-J. Hwang, H. Dai, *Nano Res.* **2015**, *9*, 28.
[83] J. Su, Y. Yang, G. Xia, J. Chen, P. Jiang, Q. Chen, *Nat. Commun.* **2017**, *8*, 1.
[84] W. Chen, J. Pei, C.-T. He, J. Wan, H. Ren, Y. Wang, J. Dong, K. Wu, W.-C. Cheong, J. Mao, X. Zheng, W. Yan, Z. Zhuang, C. Chen,

Q. Peng, D. Wang, Y. Li, W. X. Chen, J. W. Wan, H. L. Ren, K. L. Wu, W. Cheong, J. J. Mao, C. Chen, Q. Peng, D. S. Wang, Y. D. Li, J. J. Pei, Z. B. Zhuang, C. He, et al., *Adv. Mater.* **2018**, *30*, 1800396.

[85] H. G. R. Monestel, I. S. Amiinu, A. A. González, Z. Pu, B. M. Mousavi, S. Mu, *Chin. J. Catal.* **2020**, *41*, 839.

[86] K. Tu, D. Tranca, F. Rodríguez-Hernández, K. Jiang, S. Huang, Q. Zheng, M.-X. Chen, C. Lu, Y. Su, Z. Chen, H. Mao, C. Yang, J. Jiang, H.-W. Liang, X. Zhuang, K. Tu, D. Tranca, K. Jiang, S. Huang, C. Lu, Z. Chen, C. Yang, X. Zhuang, Y. Su, F. Rodríguez-Hernández, Q. Zheng, J. Jiang, M. Chen, H. Liang, H. Mao, *Adv. Mater.* **2020**, *32*, 2005433.